Biomechanics and Modeling in Mechanobiology (2021) 20:1833–1850
https://doi.org/10.1007/s10237-021-01479-9

ORIGINAL PAPER

Incorporating fiber recruitment in hyperelastic modeling of vascular tissues by means of kinematic average

Jia Lu[1] · Xuehuan He[1]

Received: 17 January 2021 / Accepted: 8 June 2021 / Published online: 26 June 2021

Abstract
We present a framework for considering the gradual recruitment of collagen fibers in hyperelastic constitutive modeling. An effective stretch, which is a response variable representing the true stretch at the tissue-scale, is introduced. Properties of the effective stretch are discussed in detail. The effective stretch and strain invariants derived from it are used in selected hyperelastic constitutive models to describe the tissue response. This construction is investigated in conjunction with Holzapfel-Gasser-Ogden family strain energy functions. The ensuing models are validated against a large body of uniaxial and bi-axial stress–strain response data from human aortic aneurysm tissues. Both the descriptive and the predictive capabilities are examined. The former is evaluated by the quality of constitutive fitting, and the latter is assessed using finite element simulation. The models significantly improve the quality of fitting, and reproduce the experiment displacement, stress, and strain distributions with high fidelity in the finite element simulation.

Keywords Fiber recruitment · Waviness distribution · Kinematic average · Vascular tissue · Structurally motivated model

1 Introduction

Elastin and collagen fibers are major determinants of passive mechanical properties of vascular tissues (Dobrin 1978). Near the ground state, collagen fibers are mostly crimped and contribute little to the mechanical response (Clark and Glagov 1985; Dingemans et al. 2000). As the load increases, the collagen fibers are gradually uncrimped and recruited into load bearing. At higher pressures, the collagen fibers are fully straightened; the tissue becomes stiffer to reinforce the vessel wall. The gradual recruitment of wavy collagen fibers is an important feature of the vascular response. It ensures that the vascular vessels are sufficiently compliant in the physiological pressure range for them to function as a conduit and at the same time, prevents them from overstretching at elevated pressures (Humphrey 2002). Studies also suggested that disease conditions such as aneurysm can alter the recruitment response. Aneurysm formation is intimately connected with loss of elastin implicated for dilation (Dobrin 1989). As such, aortic aneurysms are collagen-rich structures (Choudhury et al. 2009; Dobrin et al. 1984; Fonck et al. 2007; Iliopoulos et al. 2009; Martyn and Greenwald 1997; Sokolis et al. 2012); their mechanical response is often associated with a quick collagen recruitment (Sugita et al. 2011; Sugita and Matsumoto 2013). A recent study by the authors' group indicated that patterns in the recruitment phase of response can be exploited to evaluate the rupture risk in ascending thoracic aortic aneurysms (Luo et al. 2018; He et al. 2021a, b). Thus, the phase of response where the collagen fibers are gradually recruited merits attention.

Since the seminal work of Fung (Fung et al. 1979; Chuong and Fung 1983), hyperelastic models have been routinely used to describe the elastic behavior of soft tissues. For the vascular system, perhaps the most popular model is the Holzapfel-Gasser-Ogden (HGO) strain energy function (SEF) and its variants (Holzapfel et al. 2004a, b; Gasser et al. 2006). See Holzapfel and Ogden (2010) for a comprehensive review and references therein. The HGO family is structurally motivated models; they are phenomenological in nature and yet they take into consideration of prominent microstructural features of the fiber network. The fiber energy is represented by functions of strain invariants

✉ Jia Lu
jia-lu@uiowa.edu

Xuehuan He
xuehuan-he@uiowa.edu

[1] Department of Mechanical Engineering, and Iowa Technology Institute, The University of Iowa, Iowa City, IA 52242, USA

that are associated with distinct modes of fiber deformation. A prominent advantage of the invariant-based formulations is that they are efficient in numerical computation. As such, the HGO family has been widely used in organ-level finite element analysis. The HGO family SEFs describe the vascular tissues generally well when the collagen fibers are sufficiently stretched. However, they are less apt in capturing the transitional response associated with the graduate recruitment of the collagen fibers.

In the literature, the gradual recruitment of collagen fibers has been considered largely within the framework of *structural constitutive model* pioneered by Lanir (1979, 1983). In this approach, the strain energy of the tissue was assumed to be the sum of the individual fiber contributions. Lanir recognized that fibers have non-uniform waviness, and proposed to model the gradual straightening by probability distribution. Orientation dispersion of the fibers was described by either the mass fractions in discrete directions or a continuous density function. Following Lanir, a number of structural models have been developed for arterial tissues; see (Wuyts et al. 1995; Hurschler et al. 1997; Zulliger et al. 2004; Roy et al. 2010; Agianniotis et al. 2011; Zeinali-Davarani et al. 2015; Sacks 2003; Fan and Sacks 2014; Cacho et al. 2007; Weisbecker et al. 2015; Wulandana and Robertson 2005; Hill et al. 2012; Hamedzadeh et al. 2018; Rachev and Shazly 2019) for a selected few. These models differ in their descriptions of the waviness probability and the forms of the single fiber energy function, but they share a distinct feature in common: the fiber stress at the tissue level is formulated by a convolution or convolution-type integral over the probability space. In some special cases the fiber stress can be obtained in closed form (Roy et al. 2010; Martufi and Gasser 2011), but in general the integral needs to be evaluated numerically. The angular dispersion is incorporated by either an integration over the unit sphere, or a direct sum over discrete directions. A full structural model considering both the recruitment and the continuous fiber dispersion, therefore, can involve a triple integral. In numerical computation, structural models could invoke numerical integrations over the probability space and angular domains at the Gauss point level. In contrast, Gauss point computation in invariant-based models entails only function evaluation. To date the structural models have been used mostly at specimen level. Only lately some structural models have been tested in 3D deformation of real structures (Fan and Sacks 2014).

In this work, we present a different framework for incorporating the fiber recruitment. The point of departure lies in that the recruitment is dealt with at *kinematics* level, separated from kinetic considerations. An *effective stretch* is introduced. The effective stretch is a tissue-scale kinematic variable that represents, in an average sense, the true stretch of the tissue after factoring out the strengthening effect. It turns out to be a smooth function of the deformation. The notion of effective stretch or strain may be implied in some structural constitutive descriptions (Roy et al. 2010; Martufi and Gasser 2011); however, it has never been elucidated in the literature, to the best knowledge of the authors. The effective stretch is then used in selected hyperelastic constitutive models to describe the tissue behavior. In this manner, the recruitment response is considered within the hyperelastic framework. Evaluation of stress follows from a systematic application of chain rule. In the present work, we focus on the HGO family SEFs. We demonstrate in detail how the Gasser-Ogden-Holzapfel (GOH) model (Gasser et al. 2006) is transformed in light of the effective stretch.

The method of characterizing the waviness distribution advocated by Rezakhaniha et al. (2012) plays a pivoting role in the present development. Rezakhaniha et al investigated collagen waviness and orientation in the arterial adventitia using confocal laser scanning microscopy. They introduced a straightness parameter, which is a physical variable that can be directly measured from experiment, to quantify the waviness of a single fiber. They found that the waviness distribution over the fiber population was well described by beta distribution. Zeinali-Davaran et al used a recruitment stretch, which is reciprocal to the straightness, to parameterize the collagen undulation and benchmarked the distribution to normal and gamma functions (Zeinali-Davarani et al. 2015). The beta distribution fits nicely into the kinematic framework adapted in this work; it allows the effective stretch to be expressed in closed form, by special functions that are directly available in common programing languages (FORTRAN, C, Matlab, Python, Mathematica, R, to name a few). This is significant for theoretical development and numerical computation.

The validity of the constitutive construction is investigated using two groups of experimental data. The first group consists of 157 sets of uniaxial stress–stretch data harvested from human ascending thoracic aortic aneurysm (ATAA) tissues (Ferrara et al. 2016, 2018). The aim of this test is to examine the descriptive capability. The data are fitted to a 1D HGO strain energy function. R^2 values from with or without the recruitment are compared. The second group contains bi-axial tension–strain data extracted from bulge-inflation test of ATAA tissue specimens. Over each specimen, 2304 curves were garnered (Davis et al. 2015, 2016; Luo et al. 2016). A subset of these data are revisited in the current study. As before, the first aim is to evaluate the descriptive capability. The tension-stretch data are fitted to a 2D GOH model, with and without the fiber recruitment. Again the fitting quality is evaluated by comparing the R^2 values. The second aim is to evaluate the predictive capability as well as the robustness in finite element simulation. To this end, finite element models are developed to simulate the inflation tests. The nodal displacements and the Gauss

point tension strain values from the finite element analysis are compared with the experimental results. Finally, a synthetic model of an aorta segment undergoing pressure-driven expansion is introduced. The goal is to evaluate the performance in 3D simulation, especially for motions where the material is compressed in some directions. As will be seen in Sect. 3, we introduce two slightly different approximations for a strain invariant in the modified 3D GOH function. In theory, they should be close. A side goal of this third test is to check whether they yield close results.

2 Theory of kinematic average

Theoretical underpinnings of the proposed kinematic average approach are presented in this section. The cornerstone is the concept of effective stretch, which is a macro-scale variable representing the true stretch of the tissue. This concept is developed in a multiscale context. At macro-scale (i.e., the tissue-scale), the deformation of a material line element is described by a macroscopic stretch. At the micro-scale (i.e., the fiber-scale), a material element is associated with a family of fibers. Each fiber has its own waviness, and thus, the true stretches that the fibers experience are different. The effective stretch is the ensemble average of the fiber-scale true stretches over the waviness distribution in the fiber family.

2.1 Waviness distribution

We use the distribution model by Rezakhaniha et al. (2012) to characterize the fiber waviness. They measured the undulation of a single fiber by a straightness parameter

$$p = \frac{L}{L_f} \tag{2.1}$$

where L is end-to-end distance of the fiber and L_f is the fiber's arclength in the ground state. The parameter takes value in (0, 1). The larger the value, the lesser the waviness. The reciprocal of p is the stretch at which the fiber becomes taut. Fibers have heterogeneous waviness. Rezakhaniha et al reported that the probability density of p was well described by beta distribution

$$\psi(p;\alpha,\beta) = \frac{p^{\alpha-1}(1-p)^{\beta-1}}{B(\alpha,\beta)}, \quad p \in (0,1) \tag{2.2}$$

where (α, β) are shape parameters, both positive and $B(\alpha,\beta) = \int_0^1 x^{\alpha-1}(1-x)^{\beta-1}\,dx$ is the beta function. If $\alpha < 1$ or $\beta < 1$, the density function is unbounded when p approaches 0 or 1. These cases are not of physical relevance for the problem in hand, and hence, we impose $\alpha \geq 1, \beta \geq 1$. The mean straightness attains a simple expression

$$E(p) = \frac{\int_0^1 p^{\alpha}(1-p)^{\beta-1}\,dp}{B(\alpha,\beta)} = \frac{\alpha}{\alpha+\beta} \tag{2.3}$$

If $\alpha > \beta$, the mean straightness is greater than 0.5 and the distribution is right-skewed (left-tailed). If $\alpha < \beta$, the mean straightness is less than 0.5. and the function skews left (right-tailed). The cumulative distribution function and its tail

$$F(x;\alpha,\beta) = \frac{\int_0^x p^{\alpha-1}(1-p)^{\beta-1}\,dp}{B(\alpha,\beta)}, F(x;\alpha,\beta,\text{upper}) = \frac{\int_x^1 p^{\alpha-1}(1-p)^{\beta-1}\,dp}{B(\alpha,\beta)} \tag{2.4}$$

will be referred in the sequel. Clearly, $F(x;\alpha,\beta) + F(x;\alpha,\beta,\text{upper}) = 1$.

2.2 True stretch of a single fiber

Consider a single fiber whose curved length is L_f and the end-to-end length is L in the reference state. When it is subjected to a stretch which makes a deformed end-to-end length l, the kinematic stretch is

$$\lambda = \frac{l}{L} \tag{2.5}$$

Considering the fiber waviness, the kinematic stretch can be decomposed into the product of a true stretch λ_t and a recruitment stretch λ_r:

$$\lambda = \lambda_t \lambda_r$$

The true stretch is a portion of stretch responsible for stress generation, while the recruitment stretch is the portion spent to uncrimp the fiber. Their values depend on whether the fiber is fully straightened or not. When $l > L_f$ (fully stretched), the effective stretch is the ratio of l over the arclength L_f, and thus

$$\lambda_t := \frac{l}{L_f} = \frac{l}{L}\frac{L}{L_f} = \lambda \cdot p \tag{2.6}$$

And the recruitment stretch is $\frac{L_f}{L} = \frac{1}{p}$. When $l \leq L_f$, the total stretch is entirely spent to un-crimp the fiber but merely

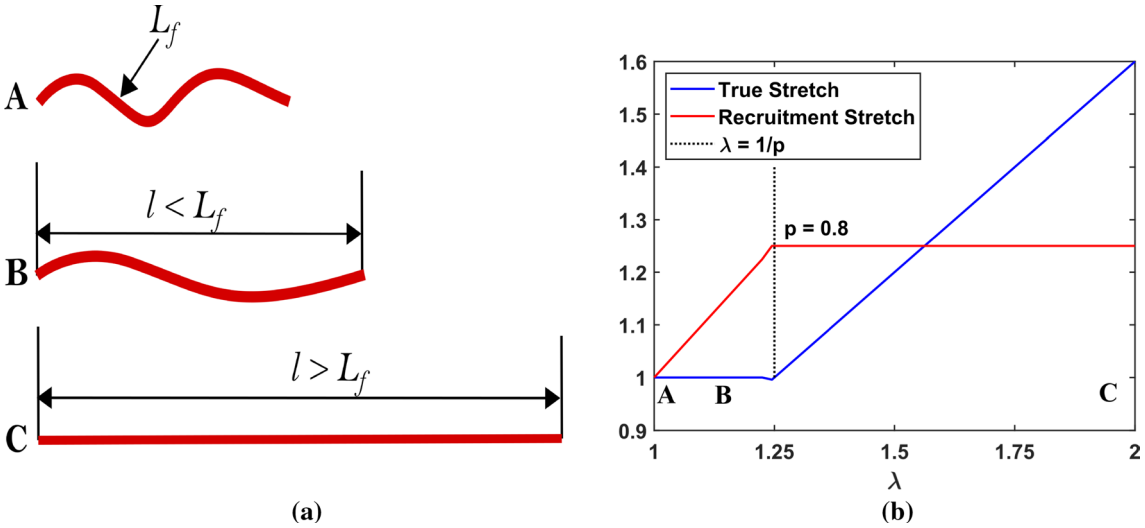

Fig. 1 **a** Schematic of fiber deformation. (A) The reference state; (B) partially uncrimped ($\lambda < \frac{1}{p}$); and (C) fully stretched ($\lambda > \frac{1}{p}$). **b** The fiber scale true stretch and the recruitment stretch plotted against λ in the case of $p = 0.8$

reduces its waviness. In this case $\lambda_r = \lambda$, and consequently $\lambda_t = 1$. These scenarios are illustrated in Fig. 1.

2.3 Effective stretch

Consider now the family of fibers contained in a material line element. When the element is subjected to a macroscopic stretch, it is natural to assume that all fibers undergo an affine deformation. Since the fibers have different waviness, they bear different values of true stretch. The effective stretch is defined as the ensemble average of the fiber-scale true stretches over the stochastic waviness distribution:

$$\bar{\lambda} = \int_0^1 \lambda_t \psi(p)\, dp \tag{2.7}$$

According to the discussion in Sect. 2.2, the true stretches in the fiber family follow the distribution:

$$\lambda_t = \begin{cases} 1 & \text{For fibers with } p \in (0, \lambda^{-1}) \\ \lambda \cdot p & \text{For fibers with } p \in (\lambda^{-1}, 1) \end{cases} \tag{2.8}$$

Taking into account this distribution, the effective stretch becomes

$$\bar{\lambda} = \int_0^{\frac{1}{\lambda}} \psi(p)\, dp + \int_{\frac{1}{\lambda}}^1 \lambda p \psi(p)\, dp \tag{2.9}$$

Upon using the beta distribution, the effective stretch reduces to a closed-form expression

$$\bar{\lambda} = F(\lambda^{-1};\alpha,\beta) + \frac{\alpha}{\alpha+\beta}\lambda F(\lambda^{-1};\alpha+1,\beta,\text{upper}) := f(\lambda;\alpha,\beta) \tag{2.10}$$

where we have used the transformation $\int_{\frac{1}{\lambda}}^1 \frac{p^\alpha(1-p)^{\beta-1}}{B(\alpha,\beta)}\, dp = F(\lambda^{-1};\alpha+1,\beta,\text{upper})\frac{B(\alpha+1,\beta)}{B(\alpha,\beta)}$ and the identity $\frac{B(\alpha+1,\beta)}{B(\alpha,\beta)} = \frac{\alpha}{\alpha+\beta}$.

The effective stretch is defined for $\lambda \geq 1$. As long as fiber kinetics is concerned, we do not need to consider $\lambda < 1$ because a crimped fiber does not generate axial resistance when compressed further if we ignore effects from bending and lateral contact. For computational purpose, however, it is necessary to define the effective

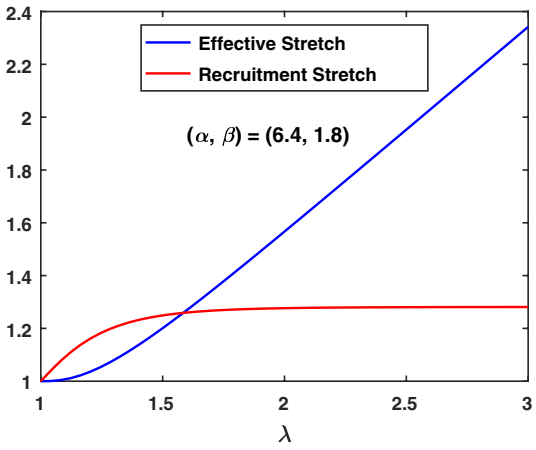

Fig. 2 Tissue-scale recruitment response in the case of $(\alpha, \beta) = (6.4, 1.8)$. The limiting slope of $\bar{\lambda}$ is $\frac{\alpha}{\alpha+\beta} = 0.78$. The asymptotic value of the recruitment stretch is $\frac{\alpha+\beta}{\alpha} = 1.28$

stretch for $\lambda < 1$. We set $\bar{\lambda} = 1$ in this case. Unless stated otherwise, subsequent discussions about $\bar{\lambda}$ are restricted to $\lambda \geq 1$.

Once $\bar{\lambda}$ is determined, the tissue-scale recruitment stretch can be defined by $\bar{\lambda}_r = \frac{\lambda}{\bar{\lambda}}$. This is a postprocess variable; it complements $\bar{\lambda}$ in describing the recruitment response. An example of the recruitment response is shown in Fig. 2. It is worth noting that both $\bar{\lambda}$ and $\bar{\lambda}_r$ are *response variables*. This is in contrast with some studies, e.g., Li and Holzapfel. (2019), which employs a tissue scale recruitment stretch as a primitive constitutive parameter.

2.4 Effective stretch in 3D deformation

In three-dimensional deformation, material elements undergo affine deformation prescribed by the local deformation gradient $\mathbf{F}$. At the continuum scale, a reference line element $d\mathbf{X}$ is mapped into $d\mathbf{x}$ via $d\mathbf{x} = \mathbf{F}d\mathbf{X}$. Let dS and $\mathbf{N}$ be the length and direction of $d\mathbf{X}$, ds and $\mathbf{n}$ be the length and direction of $d\mathbf{x}$, the mapping is written as $\mathbf{n}ds = \mathbf{F}\mathbf{N}dS$. The kinematic stretch of the element is

$$\lambda := \frac{ds}{dS} = \sqrt{\mathbf{N} \cdot \mathbf{C}\mathbf{N}} \tag{2.11}$$

where $\mathbf{C} = \mathbf{F}^T\mathbf{F}$ is the Green–Lagrangian tensor. Note that λ is a function of $\mathbf{F}$ and $\mathbf{N}$ and when necessary it will be denoted as $\lambda(\mathbf{F}, \mathbf{N})$. At the fiber-scale, a material line element is associated with a subfamily of fibers whose end-to-end vectors fall in a small cone around the direction $\mathbf{N}$. The ensemble average over this subfamily yields the effective stretch in that direction. Thus, in 3D case, the effective stretch is a function of $\mathbf{F}$ and $\mathbf{N}$; it is defined by

$$\bar{\lambda}(\mathbf{F}, \mathbf{N}; \alpha, \beta) = f(\lambda(\mathbf{F}, \mathbf{N}); \alpha, \beta) \tag{2.12}$$

When the context is clear, we will drop either $\mathbf{F}$, or $\mathbf{N}$, or (α, β), or all, from the argument list. It is worth noting that in general, the waviness distribution can vary with direction (anisotropic waviness). In this work, we assume that it is the same in all directions (isotropic waviness). This assumption is consistent with the findings in Rezakhaniha et al. (2012) which observed that the fiber straightness parameters in the arterial adventitia do not depend on the mean orientation of the fibers.

2.5 Properties of $\bar{\lambda}$

1. $\bar{\lambda}(1) = 1, 1 < \bar{\lambda} < \lambda \; \forall \lambda > 1$.
2. $\bar{\lambda}$ is a strictly increasing function;
3. $\lim_{\lambda \to \infty} \bar{\lambda}'(\lambda) = \frac{\alpha}{\alpha+\beta}$;
4. $\bar{\lambda}'(1) = 0$;
5. In 3D deformation, $\bar{\lambda}$ is a convex function of $\mathbf{F}$.

Proofs are presented in Appendix 1. These properties are essential for modeling the gradual recruitment of fibers. The first property ensures that there is no spurious compression. The second property guarantees that there is no spurious unloading. The third property is intuitive; it indicates that at large strains the effective stretch is the total stretch scaled by the mean straightness. The fourth property ensures that the transition from the undulated state to load bearing is smooth. The fifth property is critical for constructing polyconvex strain energy functions (Hartmann and Neff 2003).

We conclude this section by a remark on the choice of waviness parameters and distribution functions. Existing studies in the literature often used the recruitment stretch $\lambda_r = \frac{L_f}{L}$, which is the reciprocal of straightness parameter p, or the straightening strain $E_s = \frac{1}{2}\left(\lambda_r^2 - 1\right) = \frac{1}{2}(p^{-2} - 1)$, to describe the undulation of a single fiber. To cite a few works, Cacho et al. (2007) and Weisbecker et al. (2015) used λ_r and beta distributions. Sacks (2003) used E_s with a Gamma distribution. Zulliger et al. (2004, 2007) and Fonck et al. (2007) used E_s with log-logistic distributions. Rodriguez et al. (2006, 2008) employed the maximum fiber length with beta distributions. The present approach (p with the beta distribution) is motivated, on the one hand, by the experimental evidence that this combination best described the experimental data (Rezakhaniha et al. 2012), and on the other hand, by the algorithmic convenience it offers. If other distribution functions were used, it would be impossible to obtain a closed-form effective stretch. In addition, the straightness parameter is defined over the canonical domain (0, 1). If λ_r or E_s were used, these parameters have to be bounded in subjectively selected intervals. However, the choice of bounds would affect the shape parameters. In some cases, the shape parameters could be very sensitive to the bounds.

3 Constitutive framework

In structure-motivated hyperelastic models for the arterial tissues, the strain energy functions are constructed as the sum of two terms: a function W_g which accounts for the contribution of ground substances, and an energy function W_f which represents the contribution of fibers

$$W = W_g(\mathbf{C}) + W_f(\mathbf{C}) \tag{3.1}$$

Here, $W_g(\mathbf{C})$ is an isotropic function and is represented by principal invariants of $\mathbf{C}$:

$$I_1 = \mathrm{tr}\mathbf{C},\ I_2 = \frac{1}{2}(I_1^2 - \mathrm{tr}\mathbf{C}^2) \tag{3.2}$$

The third invariant $I_3 = \det \mathbf{C}$ does not present because of incompressibility. The Cauchy stress is determined to within a hydrostatic pressure. In numerical computation, a volumertic term $U(J)$ with $J = \det \mathbf{F}$, or a penalty function $p(J-1)$, would be augmented. Note that p is the hydrostatic pressure and it should not be confused with the straightness parameter used earlier. The fiber energy function is anisotropic. Vascular tissues typically contain several distinct families of fibers, each identified by a preferred direction $\mathbf{M}_i$. To reflect the fiber structure, most structurally motivated models chose to represent the fiber energy function using some of the following invariants

$$I_1,\ I_2,\ J_1,\ J_2, \cdots, J_N,\ K_1\ K_2, \cdots, K_N \tag{3.3}$$

where $\{J_i := \mathbf{C} : \mathbf{M}_i \otimes \mathbf{M}_i\}_{i=1}^N$ are squared stretches in each preferred direction, and $\{K_i := J^2\mathbf{C}^{-1} : \mathbf{M}_i \otimes \mathbf{M}_i\}_{i=1}^N$ are the (squared) area stretches in planes transverse to the fiber directions. The subgroup

$$I_1,\ J_1,\ J_2, \cdots, J_N \tag{3.4}$$

are line stretch-based measures; J_I's are squared stretches in the fiber directions and I_1 is the average squared stretches (modulo a factor of 3) over all directions. It can be formulated by the spherical integral

$$I_1 = \frac{3}{4\pi}\int_{S^2} \lambda^2(\mathbf{M})\, da \tag{3.5}$$

where S^2 is the surface of the unit sphere and da in an infinitesimal area element. In spherical coordinates, $da = \sin\phi d\phi d\theta$, $\mathbf{M} = \cos\theta\sin\phi\mathbf{E}_1 + \sin\theta\sin\phi\mathbf{E}_2 + \cos\phi\mathbf{E}_3$, and $\lambda^2(\mathbf{M}) = \mathbf{C} : \mathbf{M} \otimes \mathbf{M}$. The invariants

$$I_2,\ K_1,\ K_2, \cdots, K_N \tag{3.6}$$

are area stretch-based measures; I_2 (to a factor of 3) is the average of squared area stretch over all directions. Most models used today are based on the line stretch measures. For this reason, we will focus on functions represented by the subgroup (3.4). Strain energy functions that involve the subgroup (3.6), such as ones considered in (Balzani et al. 2006), will be dealt in a more general setting where an effective deformation tensor will be introduced.

Generally speaking, the proposed framework for considering the fiber recruitment amounts to replacing the invariants (3.4) in W_f with their counterparts

$$\bar{I}_1,\ \bar{J}_1, \bar{J}_2, \cdots, \bar{J}_N \tag{3.7}$$

while keeping W_g intact. Here, $\{\bar{J}_I = f^2(\sqrt{J_I})\}_{I=1}^N$ are the squared effective stretches of the corresponding fiber stretches, and $\bar{I}_1$ is the spherical average of squared effective stretches

$$\bar{I}_1 = \frac{3}{4\pi}\int_{S^2} \bar{\lambda}^2(\mathbf{M})\, da \tag{3.8}$$

In what follows we demonstrate the modification to the energy function of the Gasser-Ogden-Holzapfel model.

Gasser-Ogden-Holzapfel model. The GOH model (Gasser et al. 2006) has been broadly adapted to describe the vascular tissue response. It is an extension of the HGO function that takes into account of the directional distribution of fibers. In the GOH model, it is assumed that the tissue contains several distinct families of fibers, as marked by their mean orientations, and fibers in each family possess certain dispersion. A particular energy function for a two fiber family tissue, wherein the fiber stiffnesses are the same while the dispersions differ, with a neo-Hookean function for the ground substance, takes the form

$$W = \underbrace{\frac{\mu_1}{2}(I_1 - 3)}_{W_g} + \underbrace{\sum_{i=1}^{2}\frac{\mu_2}{4\gamma}\left(e^{\gamma(I_{ki}-1)^2} - 1\right)}_{W_f} \tag{3.9}$$

Here, $I_{\kappa i}$ is a weighted average of squared stretches in the i-th family considering the angular dispersion:

$$I_{\kappa i} = \frac{1}{4\pi}\int_{S^2} \rho(\phi,\theta)\lambda^2(\mathbf{M})\, da \tag{3.10}$$

where ρ is the orientation density function, normalized such that $\frac{1}{4\pi}\int_{S^2}\rho\, da = 1$. Under the assumption that ρ depends only on ϕ, and letting $\kappa_i = \frac{1}{4}\int_0^\pi \rho(\phi)\sin^3\phi d\phi$, the invariant reduces to

$$I_{\kappa i} = \kappa_i I_1 + (1 - 3\kappa_i)J_i, \quad J_i = \mathbf{M}_i \cdot \mathbf{C}\mathbf{M}_i \tag{3.11}$$

where $\mathbf{M}_i$ is the preferred direction of the i-th family. The parameter κ_i thus represents the dispersion. When $\kappa_i = 0$, all fibers are aligned in the preferred direction. When $\kappa_i = \frac{1}{3}$, the fibers are randomly distributed, giving an isotropic response. When $\kappa_i = \frac{1}{2}$, the fibers are concentrated on the transverse plane and randomly distributed thereon.

Considering the fiber recruitment, we define

$$\bar{I}_{\kappa i} = \frac{1}{4\pi}\int_{S^2} \rho(\phi,\theta)\bar{\lambda}^2\, da \quad \text{with} \quad \frac{1}{4\pi}\int_{S^2}\rho(\phi,\theta)\, da = 1 \tag{3.12}$$

To facilitate numerical computation, we approximate the integral using Lebedev quadratures, which are designed to exactly integrate polynomials up to a certain order over the unit sphere (Lebedev 1976). A 6-point and a 14-point quadratures are recoded in Appendix 2. Some higher-order formulas can be found in (Lebedev 1975, 1977). To this

end we choose a local basis $\{\mathbf{E}'_I\}_{I=1}^3$ (called the fiber basis hereafter) such that $\mathbf{E}'_3$ aligns with the fiber direction $\mathbf{M}_i$. The other two basis vectors can be chosen with the aid of anatomic information. For a two-family model, $\mathbf{E}'_1$ is set to lie in the fiber plane. In this case $\mathbf{E}'_2$ naturally points to the thickness direction. To start with, we employ the six point quadrature. The integration points are taken to be the vertices of the local basis vectors, $\{\pm\mathbf{E}'_1, \pm\mathbf{E}'_2, \pm\mathbf{M}_i\}$. The weights are uniform and equal to $\frac{4\pi}{6}$. This gives

$$\bar{I}_{\kappa i} = \frac{1}{3}\big(\rho(\mathbf{E}'_1)\bar{\lambda}^2(\mathbf{E}'_1) + \rho(\mathbf{E}'_2)\bar{\lambda}^2(\mathbf{E}'_2) + \rho(\mathbf{M}_i)\bar{\lambda}^2(\mathbf{M}_i)\big) \tag{3.13}$$

The normalization condition, discretized by the same scheme, yields

$$\frac{1}{3}\big(\rho(\mathbf{E}'_1) + \rho(\mathbf{E}'_2) + \rho(\mathbf{M}_i)\big) = 1 \tag{3.14}$$

Under the assumption that ρ depends only on the meridional angle ϕ, $\rho(\mathbf{E}'_1) = \rho(\mathbf{E}'_2)$. Let $\frac{\rho(\mathbf{E}'_1)}{3} = \kappa$, we obtain

$$\bar{I}_{\kappa i} = \kappa(\bar{\lambda}^2(\mathbf{E}'_1) + \bar{\lambda}^2(\mathbf{E}'_2)) + (1-2\kappa)\bar{\lambda}^2(\mathbf{M}_i) \tag{3.15}$$

The parameter κ retains its original caliber. When the fibers are randomly distributed in all directions ($\rho = 1$), $\kappa = \frac{1}{3}$. When the fibers align perfectly with $\mathbf{M}_i$, $\rho(\mathbf{E}'_1) = \rho(\mathbf{E}'_2) = 0$ and thus $\kappa = 0$. When the fibers fall on the transverse plane, $\rho(\mathbf{M}_i) = 0$; upon using the discretized normalization condition and the randomness assumption we conclude $\kappa = \frac{1}{2}$.

With the new invariant, the energy function becomes

$$W = \frac{\mu_1}{2}(I_1 - 3) + \sum_{i=1}^{2}\frac{\mu_2}{4\gamma}\left(e^{\gamma(\bar{I}_{ki}-1)^2} - 1\right) \tag{3.16}$$

Since the ground substance term remains intact, we will omit it in the discussion and focus on the fiber response only.

The fiber stress $\mathbf{S}_f := 2\frac{dW_f}{d\mathbf{C}}$ is

$$\mathbf{S}_f = \sum_{i=1}^{2}\mu_2 e^{\gamma(\bar{I}_{ki}-1)^2}(\bar{I}_{ki}-1)\left(\kappa_i\left(\sum_{I=1}^{2}\frac{d(\bar{\lambda}^2(\mathbf{E}'_I))}{d(\lambda^2(\mathbf{E}'_I))}\mathbf{E}'_I\otimes\mathbf{E}'_I\right) + (1-2\kappa_i)\frac{d\bar{J}_i}{dJ_i}\mathbf{M}_i\otimes\mathbf{M}_i\right) \tag{3.17}$$

The material tangent tensor and Cauchy response functions are recorded in Appendix3.

Alternative representation of $\bar{I}_\kappa$. Alternatively, $\bar{I}_\kappa$ can be constructed from the reduced form (3.11) by replacing I_1 with $\bar{I}_1$ and J_i with $\bar{J}_i$:

$$\bar{I}_{ki} = \kappa_i\bar{I}_1 + (1-3\kappa_i)\bar{J}_i, \quad \bar{J}_i = f^2(\sqrt{J_i}) \tag{3.18}$$

where $\bar{I}_1$ is defined in (3.8). In numerical computation, the integral is approximated by a six-point Lebedev quadrature. The integration points are taken to be the vertices of the principal vectors, $\{\pm\mathbf{N}_I\}_{I=1}^3$. At these points $\bar{\lambda}(\pm\mathbf{N}_I) = f(\lambda_I) := \bar{\lambda}_I$ where λ_I's are the principal stretches. This gives

$$\bar{I}_1 = \sum_{I=1}^{3}\bar{\lambda}_I^2 \tag{3.19}$$

The ensuing stress functions are recorded in Appendix 3.

Note that the invariant $\bar{I}_\kappa$ in (3.15) can be written as

$$\bar{I}_\kappa = \kappa(\bar{\lambda}^2(\mathbf{E}'_1) + \bar{\lambda}^2(\mathbf{E}'_2) + \bar{\lambda}^2(\mathbf{M})) + (1-3\kappa)\bar{\lambda}^2(\mathbf{M}) \tag{3.20}$$

Comparing with (3.18), the difference is that the invariant $\bar{\lambda}_1^2 + \bar{\lambda}_2^2 + \bar{\lambda}_3^2$ is replaced by $\bar{\lambda}^2(\mathbf{E}'_1) + \bar{\lambda}^2(\mathbf{E}'_2) + \bar{\lambda}^2(\mathbf{M})$. They are two different approximations of $\bar{I}_1$. Without fiber recruitment they are exactly the same. It is expected that $\bar{\lambda}^2(\mathbf{E}'_2) + \bar{\lambda}^2(\mathbf{E}'_3) + \bar{\lambda}^2(\mathbf{M}) \approx \bar{\lambda}_1^2 + \bar{\lambda}_2^2 + \bar{\lambda}_3^2$.

Note that $\bar{I}_\kappa$ defined in (3.15) is no longer an invariant *per se* because it depends on the choice of fiber basis. Nonetheless, it leads to a simpler computation. These two formulations are compared in a 3D finite element simulation reported later.

4 Validation and verification

4.1 Uniaxial response of ATAA tissue

By courtesy of Dr. Auricchio, uniaxial stress–stretch data of ATAA tissues collected at his laboratory were made available to this study. The experimental protocols were documented in Ferrara et al. (2016, 2018). A total of 187 specimens were excised from 68 patients. From each specimen, a stretch-stress curve was obtained. Through pre-screening, 30 curves deemed too noisy were excluded from this study. We elect to describe the response using a 1D HGO energy function

$$W = \frac{\mu_1}{2}\left(\lambda^2 + \frac{2}{\lambda} - 3\right) + \frac{\mu_2}{4\gamma}\left(e^{\gamma(\lambda^2-1)^2} - 1\right) \tag{4.1}$$

The first term, which represents the ground substance contribution, is reduced from the neo-Hookean energy function $\frac{\mu_1}{2}(I_1 - 3)$ upon imposing the condition $\lambda_2 = \lambda_3 = \frac{1}{\sqrt{\lambda}}$, where λ_2 and λ_3 are the principal stretches occurring in the transverse plane. It is assumed that the tissue strip contracted isotropically in lateral directions. The second term is the fiber energy, and is defined for $\lambda \geq 1$ only. The Cauchy stress follows from the formula $\sigma = \lambda\frac{dW}{d\lambda}$. Without considering the fiber recruitment,

$$\sigma = \mu_1(\lambda^2 - \lambda^{-1}) + \mu_2 e^{\gamma(\lambda^2-1)^2}(\lambda^4 - \lambda^2) \tag{4.2}$$

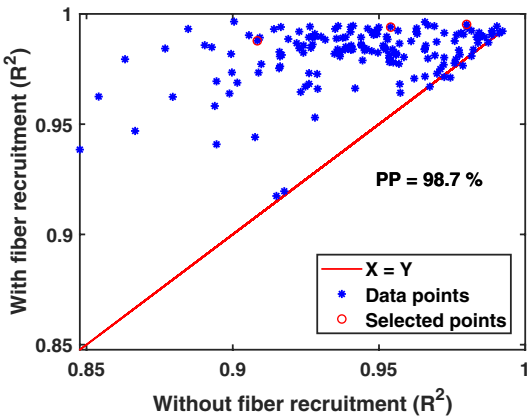

Fig. 3 Comparison of R^2 values with and without fiber recruitment in all 157 samples. Each dot represents a sample. The abscissa is the R^2 value without fiber recruitment; the ordinate is the corresponding value with fiber recruitment. PP: percentage pf points which show improvement in the R^2 value

With the fiber recruitment, the stretch λ in the second term is replaced by $\bar{\lambda}$. This gives

$$\sigma = \mu_1(\lambda^2 - \lambda^{-1}) + \mu_2 e^{\gamma(\bar{\lambda}^2-1)^2}(\bar{\lambda}^3 - \bar{\lambda})\lambda\bar{\lambda}'(\lambda) \tag{4.3}$$

The stress–strain data were fitted to both the recruitment model (Eq. (4.3)) and the original model (Eq. (4.2)). Optimized material parameters were determined by minimizing the sum of square difference between the experimental stress values and the model predictions. For the recruitment model, the parameters include the elastic properties (μ_1, μ_2, γ) and the waviness parameters (α, β). The latter are absent in the original model. These parameters were constrained such that $(\mu_1, \mu_2, \gamma) > 0, 1 \le (\alpha, \beta) \le 100$. Since the goal is not to obtain the constitutive parameters, the parameters are not generally reported.

Improvement in fitting quality. The R^2 values of all 157 samples are compared in Fig. 3. The percentage of points (PP) which show improvement in the R^2 value reaches 98.7%. Clearly, the fitting quality are universally improved when the recruitment is considered.

Figure 4 presents three examples of fitted curves; the corresponding points are marked with red circles in Fig. 3. The fiber waviness parameters (α, β), and the R^2 values from both models, are annotated on the figure. The first example is a representation of the majority of cases. The improvement is garnered in the toe region. This is the region where the graduate fiber recruitment takes place. The original model categorically over-predicts the stress, resulting a curve that lies above the experimental data points. The over-stress is rectified by using the effective stretch. The second example is an extreme case in this category. For this sample, the fibers are predicted to be nearly straight ($E(p) = 0.98$). In this case, the energy functions with or without recruitment would perform almost identically. It so happens that the original model already fits the data very well and thus little is gained from the recruitment consideration. The third example reveals another

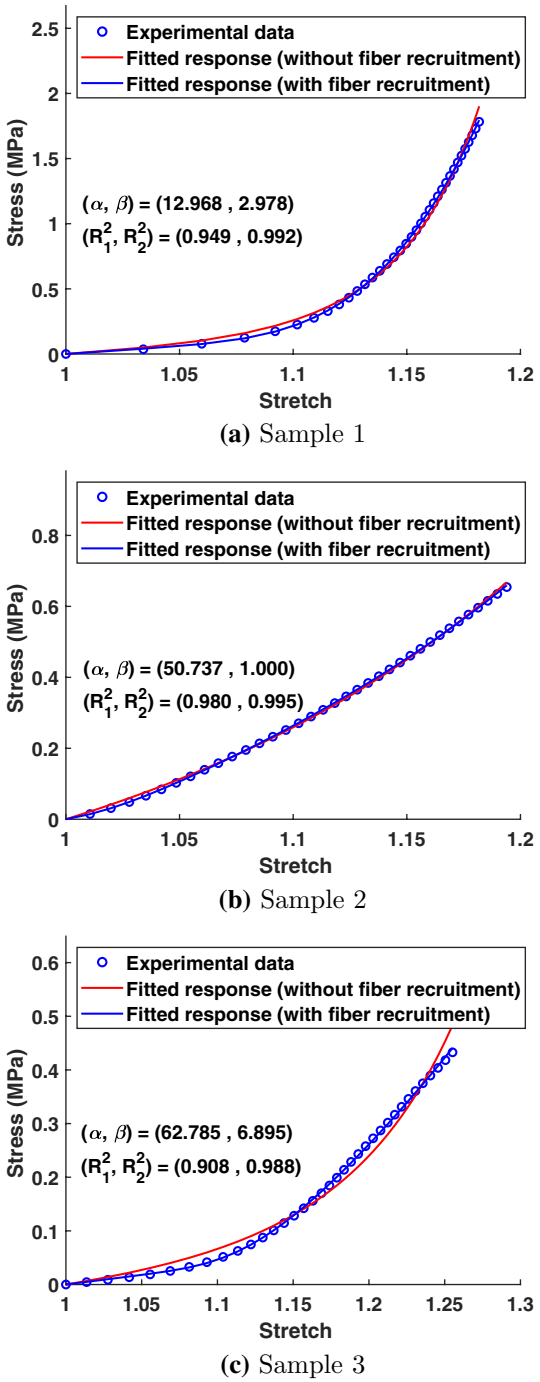

(a) Sample 1

(b) Sample 2

(c) Sample 3

Fig. 4 Fitted response curves from three samples. (α, β): Fitted waviness parameters. (R_1^2, R_2^2): R^2 values without and with considering the fiber recruitment, respectively

avenue the improvement is reaped. In this example, the original exponential function fails to fit well in both the low strain and the higher strain regions. When the recruitment is considered, the parameter γ comes out practically zero ($\gamma = 1.24\text{e}-08$, as opposed to $\gamma = 2.49$ without fiber recruitment). This suggests that the strain energy is effectively a quadratic function of the effective strain. In other words, when the straightening effect is considered, the fiber stress (in terms of the second Piola–Kirchhoff stress) is a linear function of the effective Green–Lagrangian strain. This linear relation is nicely captured by the recruitment model.

4.2 Bulge-inflation tests of ATAA tissue

In collaboration with Dr. Avril, our teams collected bi-axial response data of ATAA tissues through bulge inflation test (Davis et al. 2015, 2016; Luo et al. 2016; Romo et al. 2014). Briefly, ATAA specimens of approximated $4 \times 4\,\text{cm}^2$ were subjected to inflation test. The specimens were loaded incrementally at 3 kPa pressure increment until rupture. The deformed configuration was recorded using Digital Image Correlation (DIC), and deforming NURBS meshes were constructed for the middle regions of the specimens surfaces. Figure 5 illustrates an example. The authors used the inverse stress analysis (Lu et al. 2007; Zhou et al. 2010; Lu et al. 2013; Lu and Luo 2016) to compute the tension distribution in each deformed state. The predicted tensions were taken to be the experimental data. The surface strains were extracted from the DIC images. In this manner, 2304 tension–strain curves were collected from each specimen. The data from two specimens are used in the present study.

Since the specimens were generally thin compared to the lateral dimensions and they underwent bulge expansion, it is reasonable to treat the material as planer. Also, it has been reported that the collage structure in ATAAs is typically disrupted (de Figueiredo Borges et al. 2008), and thus, there is no compelling reason to assume the existence of directionally distinct families of fibers. For these reasons, a 2D material model reduced from the GOH function, which considers only one fiber family, is employed:

$$W = \frac{1}{2}(I_1 + I_2^{-1} - 3) + \frac{\mu_2}{4\gamma}\left(e^{\gamma(I_k-1)^2} - 1\right) \tag{4.4}$$

The first term is associated with the ground substance and is reduced from the neo-Hookean function $\frac{\mu_1}{2}(\lambda_1^2 + \lambda_2^2 + \lambda_3^2 - 3)$ upon substituting $\lambda_3 = \lambda_1^{-1}\lambda_2^{-1}$ from the incompressibility condition. Note that the deformation tensor $\mathbf{C}$ is 2×2, and $I_1 = \text{tr}\mathbf{C} = \lambda_1^2 + \lambda_2^2$ is the first principal invariant, where (λ_1, λ_2) are the in-plane principal stretches. $I_2 = \lambda_1^2\lambda_2^2$ is the second principal invariant. The second term accounts for the fiber contribution. It is assumed that the fibers are distributed symmetrically around a preferred direction $\mathbf{M}$, with a certain degree of angular dispersion. The invariant I_k is the planer average of squared fiber stretches weighted by the directional density. Without considering the recruitment, I_κ has the form

$$I_\kappa = \kappa I_1 + (1 - 2\kappa)J_1, \quad J_1 = \mathbf{M} \cdot \mathbf{CM} \tag{4.5}$$

where $\kappa \in [0, 0.5]$ is the dispersion parameter. When $\kappa = 0.5$, the fibers are randomly distributed, giving an isotropic response. When $\kappa = 0$, all fibers are perfectly aligned in the direction $\mathbf{M}$. When $0 < \kappa < 0.5$, the response is planar orthotropic. See Holzapfel and Ogden (2010). The second Piola–Kirchhoff stress is

$$\mathbf{S} = \mu_1(\mathbf{I} - I_2^{-1}\mathbf{C}^{-1}) + \mu_2 e^{\gamma(I_k-1)^2}(I_k - 1)(\kappa\mathbf{I} + (1 - 2\kappa)\mathbf{M} \otimes \mathbf{M}) \tag{4.6}$$

where $\mathbf{I}$ is the 2×2 identity tensor. With the recruitment, I_κ is replaced by

$$\bar{I}_\kappa = \kappa\bar{J}_\perp + (1 - \kappa)\bar{J}_1, \quad \bar{J}_\perp = \bar{\lambda}^2(\mathbf{M}_\perp),\ \bar{J}_1 = \bar{\lambda}^2(\mathbf{M}) \tag{4.7}$$

where $\mathbf{M}_\perp$ the perpendicular direction. Consequently,

$$\mathbf{S} = \mu_1(\mathbf{I} - I_2^{-1}\mathbf{C}^{-1}) + \mu_2 e^{\gamma(\bar{I}_k-1)^2}(\bar{I}_k - 1)\left(\kappa\frac{d\bar{J}_\perp}{dJ_\perp}\mathbf{M}_\perp \otimes \mathbf{M}_\perp + (1 - \kappa)\frac{d\bar{J}_1}{dJ_1}\mathbf{M} \otimes \mathbf{M}\right) \tag{4.8}$$

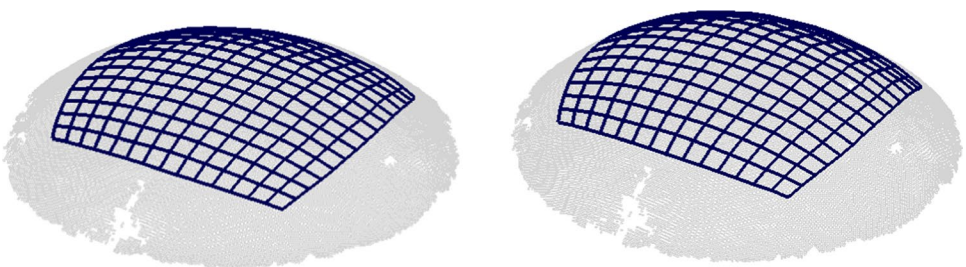

Fig. 5 NURBS mesh superimposed on the DIC point cloud at pressures 12 KPa (**left**) and 48 KPa (**right**)

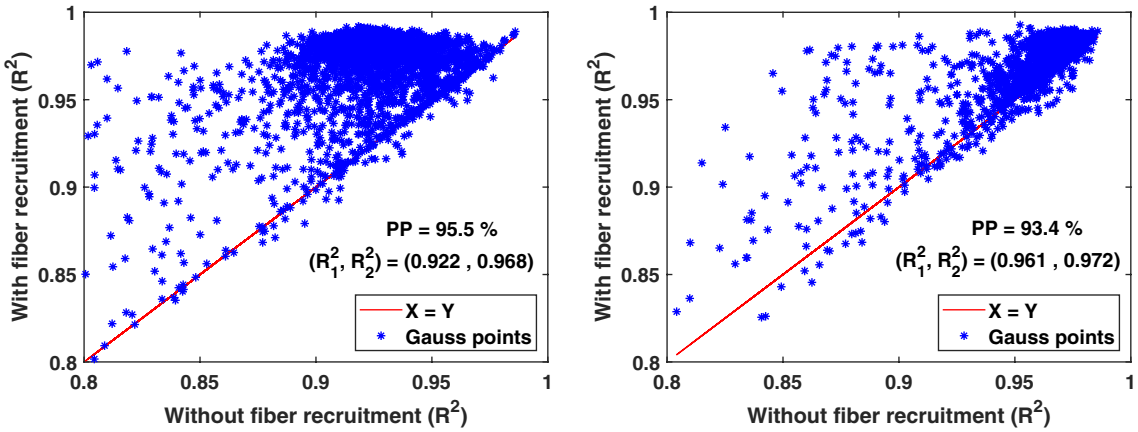

(a) Specimen 1 **(b)** Specimen 2

Fig. 6 Pointwise R^2 values with and without considering the fiber recruitment. The abscissa is the value without fiber recruitment, and the ordinate is the value with the recruitment. The PP values are the percentage of points at which the fitting quality improves. (R_1^2, R_2^2): R^2 values without and with fiber recruitment, respectively

Table 1 Statistics of the $E(p)$ distributions: means±standard deviations (SD), medians, and inter-quartile ranges $[Q1, Q3]$ with $Q1$ and $Q3$ being the 25th and the 75th percentiles, respectively

Variable		Mean ± SD	Median	[Q1, Q3]
Specimen	1	0.891 ± 0.074	0.912	[0.851, 0.951]
	2	0.928 ± 0.103	0.976	[0.854, 0.984]

The material tensor can be readily obtained by reduction from the 3D case.

4.2.1 Pointwise identification of material properties

The constitutive parameters are determined by minimizing the sum of the squares difference between the tension components computed from the inverse stress analysis (the *experiment values*) and the model predictions. All three components are included. The data are fitted to stress functions (4.6) and (4.8). For (4.8), the constitutive parameters include $(\alpha, \beta, \mu 1, \mu 2, \gamma, \theta, \kappa)$, while for (4.6) the waviness parameters are absent. The following constraints are imposed: $(\mu 1, \mu 2, \gamma) > 0$, $0 \le \theta \le \pi$, $0 \le \kappa \le 0.5$, and $1 \le (\alpha, \beta) \le 100$. The fitting is carried out *individually at every Gauss point*, to obtain the heterogeneous property distributions. Again, the parameters are not generally reported as the goal is to compare the fitting qualities.

Improvement in fitting quality. Figure 6 depicts the pointwise R^2 values associated with the stress functions (4.6) and (4.8) in Specimens 1 and 2. Each subfigure corresponds to a specimen and contains 2304 data points. The mean R^2 values (R_2^2: with fiber recruitment; R_1^2: without) and the

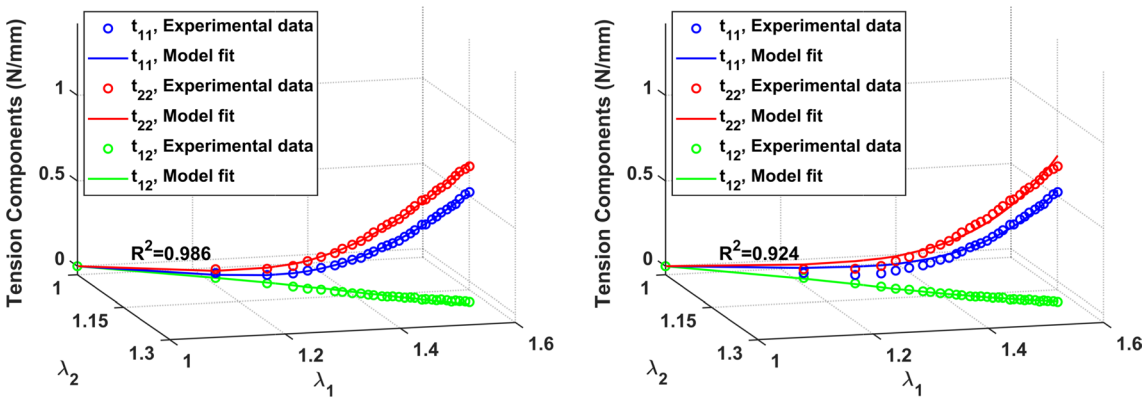

Fig. 7 Tension-stretch curves at a Gauss point, obtained with (left) and without (right) considering the recruitment. (t_{11}, t_{22}, t_{12}): components of tension in the principal strain axes. Note that t_{12} is nonzero, although small. Without considering the recruitment, t_{11} and t_{22} curves lie above the experimental points in the low strain region

PP values are also presented. Overall the fitting quality is improved when taking into account the fiber recruitment, with PP values greater than 93% for both specimens. Without recruitment, the fitting quality in Specimen 1 ($R_1^2 = 0.922$) is poorer than in Specimen 2 ($R_1^2 = 0.961$). With the recruitment, the R_2^2 values are similar. Specimen 1 shows a larger margin of improvement. We submit that the difference in the margin relates directly to the waviness; the wavier the specimen, the greater the improvement. To verify this, statistics of $E(p)$ distribution in each specimen are summarized in Table 1. Clearly, fibers in Specimen 1 are wavier, in congruence with the conjecture.

Figure 7 presents fitted tension components at a Gauss point in Specimen 1 for visual inspection. To facilitate plotting, the tension components are rotated to the principal strain axes, and plotted against the principal stretches. As in the 1D case, the fitted curves without recruitment fail to accurately capture the response in the low strain region. The components t_{11} and t_{22} lie above the experimental points. In contrast, the recruitment model fits the experimental data very well over the entire stretch range.

4.2.2 Forward validation

Finite element models are developed to simulate the inflation tests. The specimens are modeled as membranes; the identified pointwise constitutive parameters are mapped back to define the heterogeneous anisotropic properties. The mesh boundary is displacement-driven, prescribed by the motion recorded by the DIC. A transverse follower pressure is applied on the specimen surface.

Contours of total displacement, total tension (i.e., the norm) and total stain are presented in Figs. 8 and 9. Figure 8 shows the finite element predictions with and without fiber recruitment at 48 KPa pressure, along with the experimental data, for Specimen 1. Figure 9 does the same for Specimen 2 at 33 KPa. It is evident that the model with the fiber recruitment reproduces the tension and strain distributions with excellent fidelity. Intricate local features are replicated. The model without recruitment captures the global patterns generally well, but fails to accurately match the local features.

To further assess the fidelity of the finite element solutions, the mean absolute percentage errors (MAPEs) of the displacement, the tension and the strain over the domain are computed at every pressure steps. The MAPE is computed according to

$$\mathrm{MAPE}(\cdot) = \frac{1}{n}\sum_{t=1}^{n}\left|\frac{E_t(\cdot) - P_t(\cdot)}{E_i(\cdot)}\right|, \tag{4.9}$$

where E_t stands for the experimental value, P_t is the finite element prediction, and n represents the number of Gauss points or nodes. The evolution of the MAPEs with pressure steps is shown in Fig. 10, where the MAPE values at 7 pressure steps were plotted. Evidently, the MAPESs from the finite element model with the fiber recruitment are far below their counterparts without the fiber recruitment, in all categories. For Specimen 1, the MAPEs of tension and strain fall below 2.5% after 40 KPa. For Specimen 2, the values are below 1% after 20 KPa. In these pressure ranges the displacement errors are near zero. The finite element models with the fiber recruitment clearly outperform the ones without.

4.3 Pressure-driven expansion of an artery segment

As alluded before, this is a synthetic example introduced to test the performance of the 3D recruitment GOH function (3.16) in finite element simulation. In Sect. 3, we introduced two approximations for the strain invariant $\bar{I}_\kappa$. The purpose of this test is to check the influence of the approximations. The constitutive parameters are obtained by fitting stress–strain data selected from the uniaxial response database employed in Sect. 4.1. A hypothetical 3D setting is assumed. The loading direction is taken to be a principal stretch (λ_l) direction. The tissue is assumed to have two families of fibers symmetrically oriented with respect to the loading direction. Considering the incompressibility, the deformation gradient is then given as $\mathbf{F} = \mathrm{diag}(\lambda_l, \lambda_t, \lambda_l^{-1}\lambda_t^{-1})$. The transverse stretch λ_t in the fiber plane is numerically identified together with constitutive parameters by minimizing the sum of the squared difference between full 3D stress components, wherein the zero stress conditions along the transverse and the thickness directions are imposed. Two sets of parameters are acquired, and both are used in the simulation. The obtained constitutive parameters are listed in Table 2.

The finite element model is shown in Fig. 11. The inner radius, wall thickness, and length are taken to be $R = 4.745$ mm, $H = 0.43$ mm, and $L = 5$ mm, respectively. Due to symmetry, only a quarter of the structure is considered. The top and bottom ends are constrained in the axial direction, and symmetry conditions are applied on the symmetry planes.

Quasi-static deformation is simulated over the pressure range of $(0, 25)$KPa. The solution converged smoothly at each time step, without any numerical issue. Pressure–radius (PR) curves are presented in Fig. 12. Two forms of stress functions, arising from the different approximations of $\bar{I}_\kappa$, are used. The PR curves are very close for both materials.

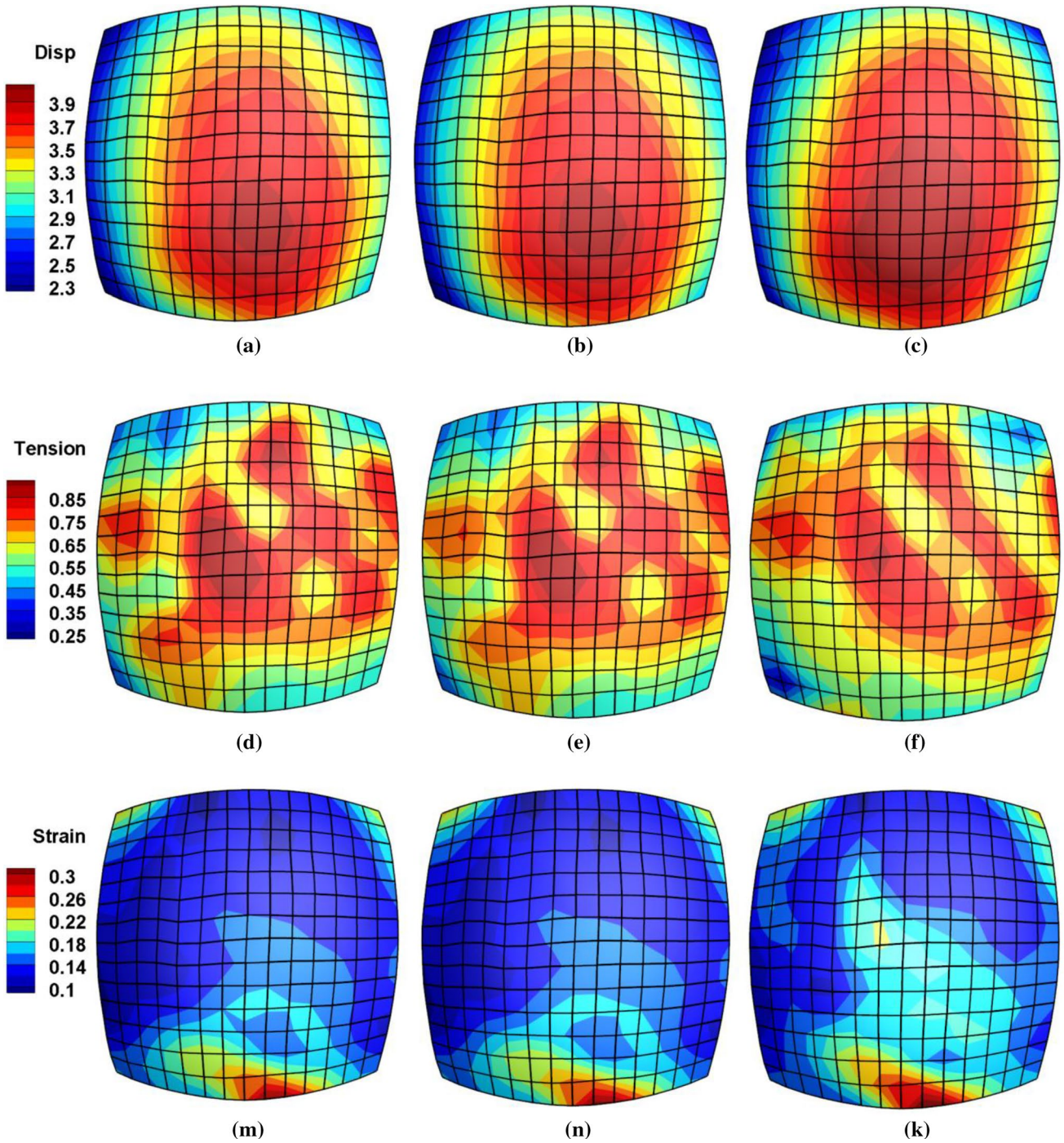

Fig. 8 Contours of the total displacement (mm, **first row**), total tension (N/mm, **second row**) and total strain (**third row**) from the experiment (**a, d, m**), finite element simulation with the recruitment (**b, e, n**), and finite element results without recruitment (**c, f, k**), at 48 KPa pressure, in Specimen 1. The experimental tension (**d**) was obtained from the inverse stress analysis

5 Concluding remarks

We presented a framework for considering the graduate recruitment of collagen fibers in hyperelastic modeling of vascular tissues. The salient feature of this approach is that the recruitment is considered at the kinematics level. The effective stretch, which is a smooth response function embedding the gradual recruitment, is the cornerstone of the construction. The effective stretch is invoked to modify strain invariants, which are then used in selected hyperelastic SEFs to model the tissue behavior. We have implemented the recruitment model in selected HGO strain energy functions. The ensuing models

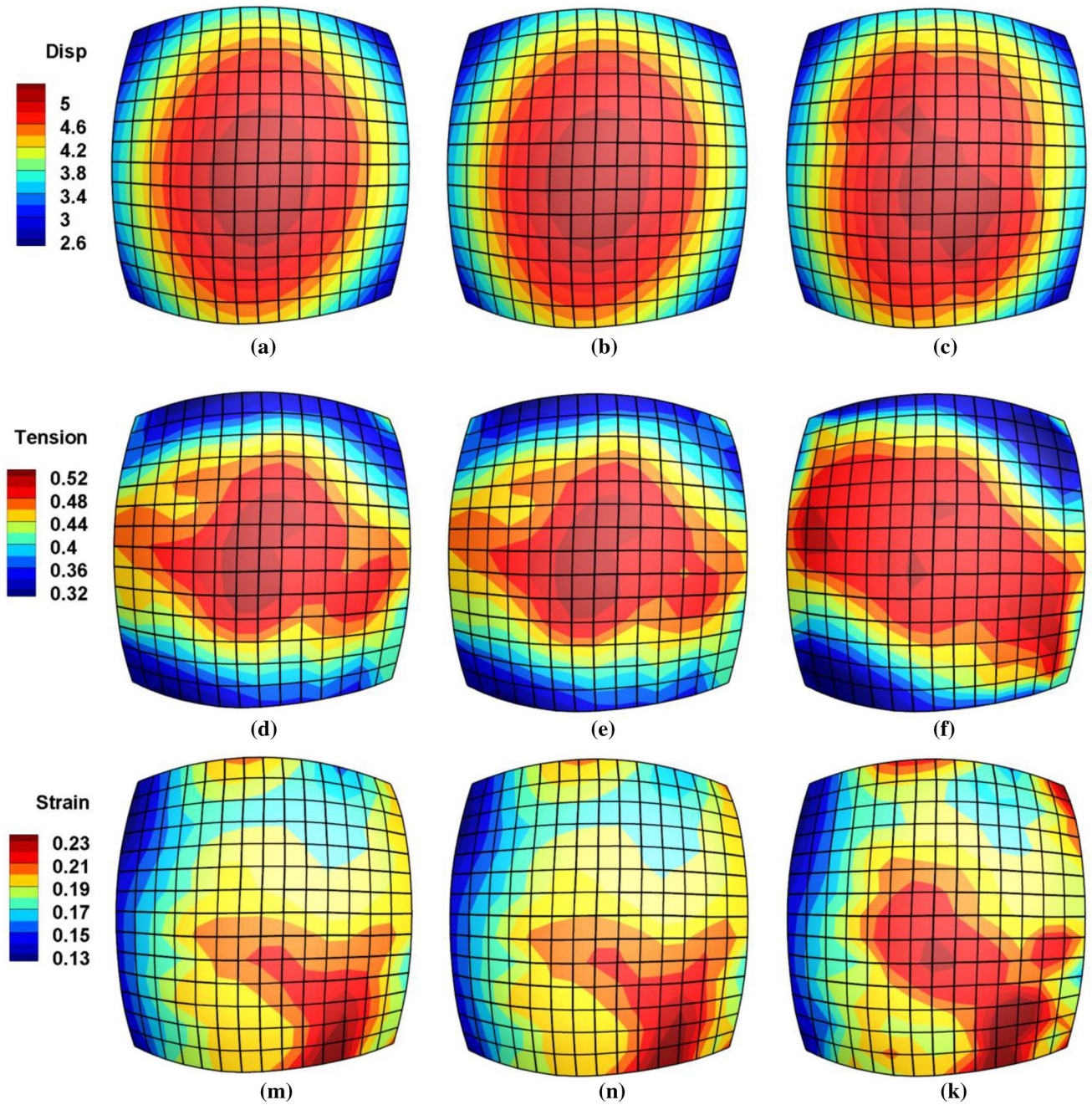

Fig. 9 Contours of the total displacement (mm, **first row**), total tension (N/mm, **second row**) and total strain (**third row**) from the experiment (**a, d, m**), finite element simulation with the recruitment (**b, e, n**), and finite element results without recruitment (**c, f, k**), at 33 KPa pressure, in Specimen 2. The experimental tension (**d**) was obtained from the inverse stress analysis

are essentially extensions of HGO family SEFs with two more parameters to take into account of the random fiber waviness. We validated this constitutive construction against experimental data. Models incorporated the fiber recruitment significantly improve the fitting quality, and overwhelmingly outperform the original models in reproducing the experimental results.

This approach permits us to consider the fiber recruitment within the hyperelastic framework. Constitutive models constructed in this way preserve the invariant formulation. They are thus efficient in numerical computation. Owing to the beta distribution, the effective stretch is expressed by incomplete beta functions which are directly available in major programing languages. We have shown that, for the modified HGO family SEFs, the stress functions entail only minor modifications to the original formulation. In addition, the construction preserves the polyconvexity of the HGO

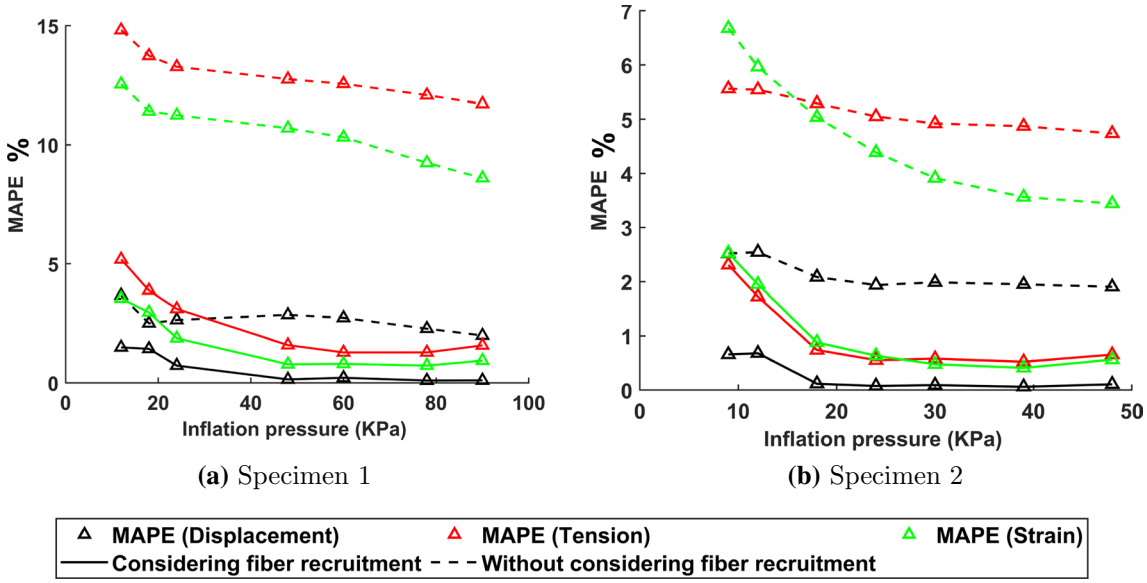

Fig. 10 Mean absolute percentage error (MAPE) of displacement (**black**), tension (**red**) and strain (**green**) at different pressure steps, from the models with the fiber recruitment (**solid line**) and without (**dash line**)

Table 2 Constitutive parameters of two material models extracted from the uniaxial database

	Parameter	α	β	$u_1(MPa)$	$u_2(MPa)$	γ	κ	$\theta(rad)$
Material model	1	62.552	2.185	0.105	4.143	82.446	0.194	0.269
	2	22.97	1.41	0.061	1.396	2.33e-4	0.122	0.424

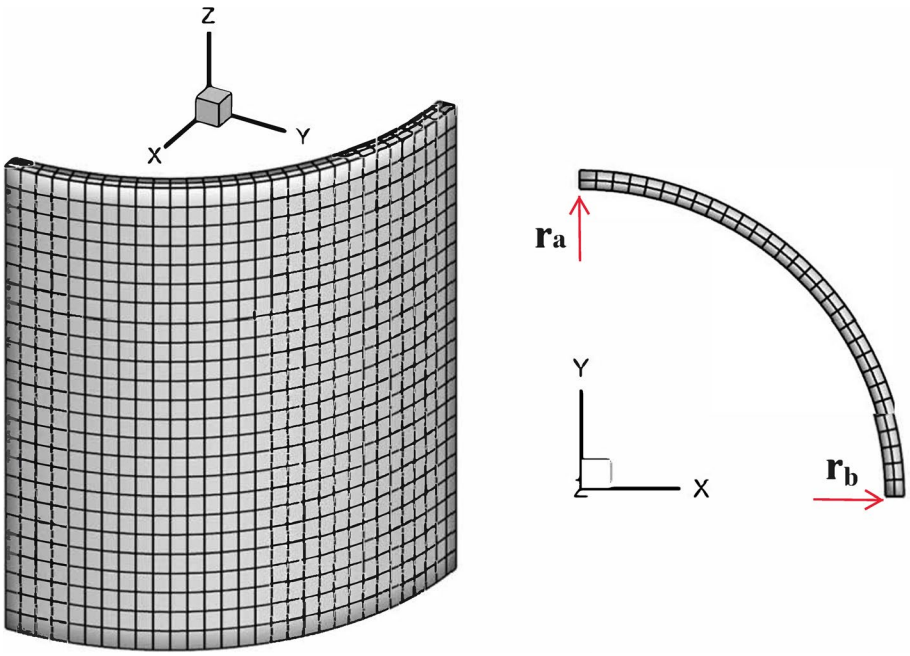

Fig. 11 Finite element mesh for the quarter model of artery segment

family SEFs, because the effective stretch is a convex function of **F**. This feature is not discussed in the main text, but it is a key factor underlying the excellent numerical stability observed in the finite element simulations.

On the other hand, since the response of a material element is formulated in terms of the average deformation of fibers, this approach is not flexible for taking into account of individual fiber behavior. The limitation should be kept in

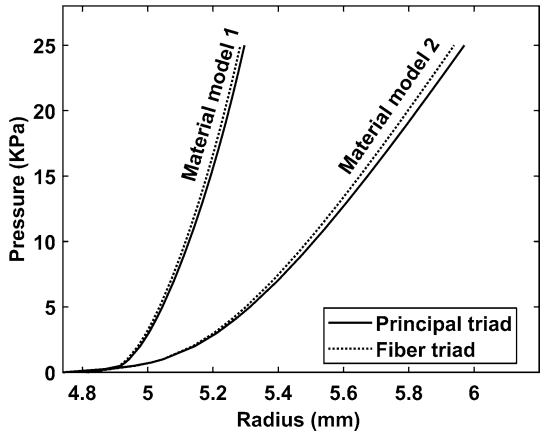

Fig. 12 Pressure–radius curves showing the influence of different definitions of $\bar{I}_\kappa$ in the global response. Solid curves: responses arising from representation of $\bar{I}_\kappa$ using the principal basis. Dashed curves: using the fiber basis

mind. Furthermore, a model constructed in this framework may inherit limitations embedded in the parent SEF. For example, the invariant I_κ in the GOH model does not differentiate extended and compressed fibers in a dispersed family, and consequently, its validity in the situations where the fibers are partially in compression becomes questionable (Lanir and Namani 2015). Several remedies have been proposed within the framework of invariant formulation (Holzapfel and Ogden 2017; Li et al. 2018). Presumably, the recruitment treatment can also be incorporated into the modified SEFs. Issues of this nature should be addressed case by case.

Lastly, it is assumed that the waviness distribution is isotropic. This assumption could be reasonable for artery adventitia (Rezakhaniha et al. 2012), but could be questionable for other vascular tissues. Anisotropic waviness distributions will be considered in future work.

Appendix 1 Proof of properties of $\bar{\lambda}$

Properties 1, 2, 3, and 4 hinge on the derivative of $\bar{\lambda}$:

$$\bar{\lambda}' = \frac{\alpha}{\alpha+\beta} F(\lambda^{-1}, \alpha+1, \beta, \text{upper}) + \frac{d}{d\lambda}\int_0^{\frac{1}{\lambda}} \frac{p^{\alpha-1}(1-p)^{\beta-1}}{B(\alpha,\beta)}\, dp + \lambda \frac{d}{d\lambda}\int_{\frac{1}{\lambda}}^1 \frac{p^{\alpha}(1-p)^{\beta-1}}{B(\alpha,\beta)}\, dp \tag{4.10}$$

A straightforward computation shows that the second and third terms cancel out, leaving

$$\bar{\lambda}' = \frac{\alpha}{\alpha+\beta} F(\lambda^{-1}; \alpha+1, \beta, \text{upper}) \tag{4.11}$$

Clearly,

$$\bar{\lambda}'(1) = 0, \quad \lim_{\lambda\to\infty} \bar{\lambda}'(\lambda) = \frac{\alpha}{\alpha+\beta} \tag{4.12}$$

Properties 3 and 4 are proved. Further, it is evident that

$$0 < \bar{\lambda}' < 1 \quad \forall \lambda \in (1, \infty) \tag{4.13}$$

and

$$\bar{\lambda}(1) = 1 \tag{4.14}$$

Properties 1 and 2 are the consequences of these results. First, $\bar{\lambda}' > 0$ indicates that $\bar{\lambda}$ is a strictly increasing function in $(1, \infty)$. Consequently,

$$\bar{\lambda}(\lambda) > \bar{\lambda}(1) = 1 \quad \forall \lambda \in (1, \infty) \tag{4.15}$$

Similarly, $\bar{\lambda}' < 1$ implies that $\bar{\lambda}(\lambda) - \lambda$ is a strictly decreasing function in $(1, \infty)$, and thus

$$\bar{\lambda}(\lambda) - \lambda < \bar{\lambda}(1) - 1 = 0 \quad \forall \lambda \in (1, \infty) \tag{4.16}$$

We thus conclude that

$$1 < \bar{\lambda}(\lambda) < \lambda \quad \forall \lambda \in (1, \infty) \tag{4.17}$$

To show that $\bar{\lambda}(\mathbf{F})$ is a convex function of $\mathbf{F}$, first observe that $\bar{\lambda}' = \int_{\frac{1}{\lambda}}^1 \frac{p^{\alpha}(1-p)^{\beta-1}}{B(\alpha,\beta)}\, dp$, and hence

$$\bar{\lambda}'' = \frac{d}{d\lambda}\int_{\frac{1}{\lambda}}^1 \frac{p^{\alpha}(1-p)^{\beta-1}}{B(\alpha,\beta)}\, dp = \frac{\left(\frac{1}{\lambda}\right)^{\alpha+2}\left(1-\left(\frac{1}{\lambda}\right)\right)^{\beta-1}}{B(\alpha,\beta)} > 0 \quad \text{for} \quad \lambda \in (1, \infty) \tag{4.18}$$

By construction, $\bar{\lambda} = 1$ for $\lambda \le 1$, which is convex. Thus, $\bar{\lambda}$ is a convex function of λ over $(0, \infty)$. It follows that

$$\bar{\lambda}(\lambda_2) - \bar{\lambda}(\lambda_1) \ge \left.\frac{d\bar{\lambda}}{d\lambda}\right|_{\lambda=\lambda_1} (\lambda_2 - \lambda_1) \quad \text{for } \lambda \in (0, \infty) \tag{4.19}$$

At the same time, $\lambda = \sqrt{\mathbf{FN}\cdot\mathbf{FN}}$ is a convex function of $\mathbf{F}$ for any fixed $\mathbf{N}$ (Hartmann and Neff 2003), so that

$$\lambda(\mathbf{F}_2) - \lambda(\mathbf{F}_1) \ge \left.\frac{d\lambda(\mathbf{F})}{d\mathbf{F}}\right|_{\mathbf{F}=\mathbf{F}_1} : (\mathbf{F}_2 - \mathbf{F}_1) \tag{4.20}$$

Combining these two inequalities and noticing $\frac{d\bar{\lambda}}{d\lambda} \geq 0$, we conclude

$$\begin{aligned}\bar{\lambda}(\mathbf{F}_2) - \bar{\lambda}(\mathbf{F}_1) &\geq \frac{d\bar{\lambda}}{d\lambda}\frac{d\lambda(\mathbf{F})}{d\mathbf{F}}\bigg|_{\mathbf{F}=\mathbf{F}_1} : \\ (\mathbf{F}_2 - \mathbf{F}_1) &= \frac{d\bar{\lambda}(\mathbf{F})}{d\mathbf{F}}\bigg|_{\mathbf{F}=\mathbf{F}_1} : (\mathbf{F}_2 - \mathbf{F}_1)\end{aligned} \tag{4.21}$$

which proves the convexity.

Appendix 2 Lebedev quadrature

Six-point quadrature

$$\frac{1}{4\pi}\int_{S^2} f\, da = \frac{1}{6}\sum_{i=1}^{6} f(\mathbf{a}_i^{(1)}), \quad \mathbf{a}_i^{(1)} = \{\pm 1, 0, 0\}, \{0 \pm 1, 0\}, \{0, 0, \pm 1\} \tag{4.22}$$

14-point quadrature

$$\frac{1}{4\pi}\int_{S^2} f\, da = \frac{1}{15}\sum_{i=1}^{6} f(\mathbf{a}_i^{(1)}) + \frac{3}{40}\sum_{i=1}^{8} f(\mathbf{a}_i^{(3)}) \tag{4.23}$$

$$\begin{aligned}\mathbf{a}_i^{(3)} = &\{\pm\frac{\sqrt{3}}{3}, \pm\frac{\sqrt{3}}{3}, \pm\frac{\sqrt{3}}{3}\}, \{\mp\frac{\sqrt{3}}{3} \pm \frac{\sqrt{3}}{3}, \pm\frac{\sqrt{3}}{3}\}, \\ &\{\pm\frac{\sqrt{3}}{3}, \mp\frac{\sqrt{3}}{3}, \pm\frac{\sqrt{3}}{3}\}, \{\pm\frac{\sqrt{3}}{3}, \pm\frac{\sqrt{3}}{3}, \mp\frac{\sqrt{3}}{3}\}\end{aligned} \tag{4.24}$$

Appendix 3 Response function of the GOH model with recruitment

The derivative of $\mathbf{S}_f$ in (3.17) to $\frac{\mathbf{C}}{2}$ yields the material tangent tensor

$$\begin{aligned}\mathbb{D}_f = \sum_{i=1}^{2}\Bigg[&2\mu_2 \frac{d\left(e^{\gamma(\bar{I}_k-1)^2}(\bar{I}_k - 1)\right)}{d\bar{I}_\kappa}\mathbf{H}_i \otimes \mathbf{H}_i \\ &+ 2\mu_2 e^{\gamma(\bar{I}_k-1)^2}(\bar{I}_k - 1)\left(\kappa\mathbb{H} + (1-2\kappa)\frac{d^2\bar{J}_i}{dJ_i^2}\mathbf{M}_i \otimes \mathbf{M}_i \otimes \mathbf{M}_i \otimes \mathbf{M}_i\right)\Bigg]\end{aligned} \tag{4.25}$$

where

$$\mathbf{H}_i = \kappa\left(\sum_{I=1}^{2}\frac{d(\bar{\lambda}^2(\mathbf{E}'_I))}{d(\lambda^2(\mathbf{E}'_I))}\mathbf{E}'_I \otimes \mathbf{E}'_I\right) + (1-2\kappa)\frac{d\bar{J}_i}{dJ_i}\mathbf{M}_i \otimes \mathbf{M}_i, \ \mathbb{H} = \sum_{I=1}^{2}\frac{d^2(\bar{\lambda}^2(\mathbf{E}'_I))}{d(\lambda^2(\mathbf{E}'_I))^2}\mathbf{E}'_I \otimes \mathbf{E}'_I \otimes \mathbf{E}'_I \otimes \mathbf{E}'_I \tag{4.26}$$

Response function from the alternative approximation of $\bar{I}_\kappa$. The stress function arising from the representation (3.18) reads

$$\mathbf{S}_f = \sum_{i=1}^{2}\mu_2 e^{\gamma(\bar{I}_{ki}-1)^2}(\bar{I}_{ki} - 1)\left(\kappa_i\bar{\mathbf{I}} + (1-3\kappa_i)\frac{d\bar{J}_i}{dJ_i}\mathbf{M}_i \otimes \mathbf{M}_i\right) \tag{4.27}$$

where $\bar{\mathbf{I}} := \frac{d\bar{I}_1}{d\mathbf{C}} = \sum_{I=1}^{3}\frac{f(\lambda_I)f'(\lambda_I)}{\lambda_I}\mathbf{N}_I \otimes \mathbf{N}_I$, and $\{\mathbf{N}_I\}_{I=1}^3$ are the principal vectors. The material tangent is

$$\begin{aligned}\mathbb{D}_f = \sum_{i=1}^{2}\Bigg[&2\mu_2 \frac{d\left(e^{\gamma(\bar{I}_k-1)^2}(\bar{I}_k - 1)\right)}{d\bar{I}_\kappa}\mathbf{H}_i \otimes \mathbf{H}_i \\ &+ 2\mu_2 e^{\gamma(\bar{I}_k-1)^2}(\bar{I}_k - 1)\left(\kappa\frac{d\bar{\mathbf{I}}}{d\mathbf{C}} + (1-3\kappa)\frac{d^2\bar{J}_i}{dJ_i^2}\mathbf{M}_i \otimes \mathbf{M}_i \otimes \mathbf{M}_i \otimes \mathbf{M}_i\right)\Bigg]\end{aligned} \tag{4.28}$$

where $\mathbf{H}_i = \kappa\bar{\mathbf{I}} + (1-3\kappa)\frac{d\bar{J}_i}{dJ_i}\mathbf{M}_i \otimes \mathbf{M}_i$. The fourth-order tensor $\frac{d\bar{\mathbf{I}}}{d\mathbf{C}}$ can be obtained by a straightforward computation.

$$\begin{aligned}\frac{d\bar{\mathbf{I}}}{d\mathbf{C}} = &\sum_{I=1}^{3}\frac{1}{2\lambda_I}\frac{d}{d\lambda_I}\left(\frac{f(\bar{\lambda}_I)f'(\bar{\lambda}_I)}{\lambda_I}\right)\mathbf{N}_I \otimes \mathbf{N}_I \otimes \mathbf{N}_I \otimes \mathbf{N}_I \\ &+ \sum_{I=1}^{3}\sum_{J>I}\frac{1}{2(\lambda_I^2 - \lambda_J^2)}\left(\frac{f(\lambda_I)f'(\lambda_I)}{\lambda_I} - \frac{f(\lambda_J)f'(\lambda_J)}{\lambda_J}\right)\mathbf{\Psi}_{IJ} \otimes \mathbf{\Psi}_{IJ}\end{aligned} \tag{4.29}$$

where $\mathbf{\Psi}_{IJ} = \mathbf{N}_I \otimes \mathbf{N}_J + \mathbf{N}_J \otimes \mathbf{N}_I$. In the limiting case of $\lambda_I \to \lambda_J$:

$$\frac{1}{\lambda_I^2 - \lambda_I^2}\left(\frac{\bar{\lambda}_I}{\lambda_I}\frac{d\bar{\lambda}_I}{d\lambda_I} - \frac{\bar{\lambda}_J}{\lambda_J}\frac{d\bar{\lambda}_J}{d\lambda_J}\right) = \frac{1}{2\lambda_I}\frac{d}{d\lambda_I}\left(\frac{f(\bar{\lambda}_I)f'(\bar{\lambda}_I)}{\lambda_I}\right) \tag{4.30}$$

Volumetric-deviatoric splitting. In finite element implementation, a multiplicative volumetric-deviatoric splitting is applied to the deformation gradient. The isochoric factor $\tilde{\mathbf{F}} = J^{-\frac{1}{3}}\mathbf{F}$ is passed to the strain energy function. A volumetric term $U(J)$ is added to energy function, giving

$$W(\mathbf{F}) = \frac{\mu_1}{2}(\mathrm{tr}\tilde{\mathbf{C}} - 3) + W_f(\tilde{\mathbf{C}}) + U(J), \quad \tilde{\mathbf{C}} = J^{-\frac{2}{3}}\mathbf{C} \tag{4.31}$$

Let $\tilde{\boldsymbol{\sigma}}$ and the $\tilde{\mathbb{C}}$ be the *algorithm* Cauchy stress and material tangent tensor arising from $W_f + W_g$, namely the response evaluating at $\mathbf{F} = \tilde{\mathbf{F}}$. The actual Cauchy stress and spatial material tensor are obtained through deviatoric projections (Simo et al. 1985) of the algorithm response, adding the contributions form $U(J)$:

$$\begin{aligned}\boldsymbol{\sigma} &= \tilde{\boldsymbol{\sigma}}_{\text{dev}} + U'(J)\mathbf{1}, \quad \text{where } \tilde{\boldsymbol{\sigma}}_{\text{dev}} = \mathbb{I}_{\text{dev}}\tilde{\boldsymbol{\sigma}} \\ \mathbb{C} &= \mathbb{I}_{\text{dev}}\tilde{\mathbb{C}}\mathbb{I}_{\text{dev}} - \frac{2}{3}\tilde{\boldsymbol{\sigma}}_{\text{dev}} \otimes \mathbf{1} - \frac{2}{3}\mathbf{1} \otimes \tilde{\boldsymbol{\sigma}}_{\text{dev}} \\ &\quad + \frac{2\text{tr}\tilde{\boldsymbol{\sigma}}}{3}\mathbb{I}_{\text{dev}} - 2U'(J)\mathbb{I} + (JU'(J))'\mathbf{1} \otimes \mathbf{1}\end{aligned} \tag{4.32}$$

where $\mathbb{I}$ and $\mathbf{1}$ are the fourth- and second-order identity tensors, $\mathbb{I}_{\text{dev}} = \mathbb{I} - \frac{1}{3}\mathbf{1} \otimes \mathbf{1}$ is the deviatoric projector.

Acknowledgements The authors would like to thank Drs. Auricchio and Avril for providing the experimental data. The work was supported by a development grant from ANSYS Inc. The support is gratefully acknowledged.

References

Agianniotis A, Rezakhaniha R, Stergiopulos N (2011) A structural constitutive model considering angular dispersion and waviness of collagen fibres of rabbit facial veins. Biomed Eng Online 10:18–18. https://doi.org/10.1186/1475-925X-10-18

Balzani D, Neff P, Schröder J, Holzapfel GA (2006) A polyconvex framework for soft biological tissues. Adjustment to experimental data. Int J Solids Struct 43(20):6052–6070. https://doi.org/10.1016/.ijsolstr.2005.07.048

Cacho F, Elbischger PJ, Rodríguez JF, Doblaré M, Holzapfel GA (2007) A constitutive model for fibrous tissues considering collagen fiber crimp. Int J Non-Linear Mech 42(2):391–402. https://doi.org/10.1016/j.ijnonlinmec.2007.02.002

Choudhury N, Bouchot O, Rouleau L, Tremblay D, Cartier R, Butany J, Mongrain R, Leask RL (2009) Local mechanical and structural properties of healthy and diseased human ascending aorta tissue. Cardiovasc Pathol 18(2):83–91. https://doi.org/10.1016/j.carpath.2008.01.001

Chuong CJ, Fung YC (1983) Three-dimensional stress distribution in arteries. J Biomech Eng 105(3):268–274. https://doi.org/10.1115/1.3138417

Clark JM, Glagov S (1985) Transmural organization of the arterial media. The lamellar unit revisited. Arteriosclerosis 5(1):19–34. https://doi.org/10.1161/01.atv.5.1.19

Davis FM, Luo Y, Avril S, Duprey A, Lu J (2015) Pointwise characterization of the elastic properties of planar soft tissues: application to ascending thoracic aneurysms. Biomech Model Mechanobiol 14:967–978. https://doi.org/10.1007/s10237-014-0646-9

Davis FM, Luo Y, Avril S, Duprey A, Lu J (2016) Local mechanical properties of human ascending thoracic aneurysms. J Mech Behav Biomed Mater 61:235–249. https://doi.org/10.1016/j.jmbbm.2016.03.025

de Figueiredo Borges L, Jaldin RG, Dias RR, Stolf NAG, Michel J-B, Gutierrez PS (2008) Collagen is reduced and disrupted in human aneurysms and dissections of ascending aorta. Hum Pathol 39(3):437–443. https://doi.org/10.1016/j.humpath.2007.08.003

Dingemans KP, Teeling Peter, Lagendijk JH, Becker AE (2000) Extracellular matrix of the human aortic media: An ultrastructural histochemical and immunohistochemical study of the adult aortic media. Anat Rec 258(1):1

Dobrin PB (1978) Mechanical properties of arteries. Physiol Rev 58(2):397–460. https://doi.org/10.1152/physrev.1978.58.2.397

Dobrin PB (1989) Patho-physiology and pathogenesis of aortic-aneurysms - current concepts. Surg Clin North Am 69(4):687–703

Dobrin PB, Baker WH, Gley WC (1984) Elastolytic and collagenolytic studies of arteries - implications for the mechanical-properties of aneurysms. Arch Surg 119(4):405–409. https://doi.org/10.1001/archsurg.1984.01390160041009

Fan R, Sacks MS (2014) Simulation of planar soft tissues using a structural constitutive model: finite element implementation and validation. J Biomech 47(9):2043–2054

Ferrara A, Morganti S, Totaro P, Mazzola A, Auricchio F (2016) Human dilated ascending aorta: Mechanical characterization via uniaxial tensile tests. J Mech Behav Biomed Mater 53:257–271. https://doi.org/10.1016/j.jmbbm.2015.08.021

Ferrara A, Totaro P, Morganti S, Auricchio F (2018) Effects of clinico-pathological risk factors on in-vitro mechanical properties of human dilated ascending aorta. J Mech Behav Biomed Mater 77:1–11. https://doi.org/10.1016/j.jmbbm.2017.08.032

Fonck E, Prod'hom G, Roy S, Augsburger L, Rufenacht DA, Stergiopulos N (2007) Effect of elastin degradation on carotid wall mechanics as assessed by a constituent-based biomechanical model. Am J Physiol Heart Circ Physiol 292(6):H2754–H2763. https://doi.org/10.1152/ajpheart.01108.2006

Fung YC, Fronek K, Patitucci P (1979) Pseudoelasticity of arteries and the choice of its mathematical expression. Am J Physiol Heart Circ Physiol 237(5):H620–H631. https://doi.org/10.1152/ajpheart.1979.237.5.H620

Gasser TC, Ogden RW, Holzapfel GA (2006) Hyperelastic modelling of arterial layers with distributed collagen fibre orientations. J R Soc Interface 3(6):15–35. https://doi.org/10.1098/rsif.2005.0073

Hamedzadeh A, Gasser TC, Federico S (2018) On the constitutive modelling of recruitment and damage of collagen fibres in soft biological tissues. Eur J Mech A/Solids 72:483–496

Hartmann S, Neff P (2003) Polyconvexity of generalized polynomial-type hyperelastic strain energy funtions for near-incompressibility. Int J Solids Struct - INT J SOLIDS STRUCT 40:2767–2791. https://doi.org/10.1016/S0020-7683(03)00086-6

He X, Avril S, Lu J (2021a) Prediction of local strength of ascending thoracic aortic aneurysms. J Mech Behav Biomed Mater 115:104284. https://doi.org/10.1016/j.jmbbm.2020.104284

He X, Avril S, Lu J (2021b) Estimating aortic thoracic aneurysm rupture risk using tension-strain data in physiological pressure range: an in vitro study. Biomech Model Mechanobiol. https://doi.org/10.1007/s10237-020-01410-8

Hill MR, Duan X, Gibson GA, Watkins S, Robertson AM (2012) A theoretical and non-destructive experimental approach for direct inclusion of measured collagen orientation and recruitment into mechanical models of the artery wall. J Biomech 45(5):762–71. https://doi.org/10.1016/j.jbiomech.2011.11.016

Holzapfel G, Gasser T, Ogden R (2004a) A new constitutive framework for arterial wall mechanics and a comparative study of material models. J Elast 61(3):1–48

Holzapfel GA, Ogden RW (2010) Constitutive modelling of arteries. Proc Royal Soc Math Phys Eng Sci 466(2118):1551–1597. https://doi.org/10.1098/rspa.2010.0058

Holzapfel GA, Ogden RW (2017) On fiber dispersion models: exclusion of compressed fibers and spurious model comparisons. J Elast 129(1–2):49–68

Holzapfel GA, Gasser TC, Ogden RW (2004b) Comparison of a multi-layer structural model for arterial walls with a fung-type model, and issues of material stability. J Biomech Eng 126(2):264–275. https://doi.org/10.1115/1.1695572

Humphrey JD (2002) Cardiovascular solid mechanics: cells, tissues, and organs. Springer, New York

Hurschler C, Loitz-Ramage B, Vanderby Jr. R (1997) A structurally based stress-stretch relationship for tendon and ligament. J Biomech Eng 119(4):392–399. https://doi.org/10.1115/1.2798284

Iliopoulos DC, Kritharis EP, Giagini AT, Papadodima SA, Sokolis DP (2009) Ascending thoracic aortic aneurysms are associated with compositional remodeling and vessel stiffening but not weakening in age-matched subjects. J Thorac Cardiovasc Surg 137(1):101–109. https://doi.org/10.1016/j.jtcvs.2008.07.023

Lanir Y (1979) A structural theory for the homogeneous biaxial stress-strain relationships in flat collagenous tissues. J Biomech 12(6):423–436. https://doi.org/10.1016/0021-9290(79)90027-7

Lanir Y (1983) Constitutive equations for fibrous connective tissues. J Biomech 16(1):1–12. https://doi.org/10.1016/0021-9290(83)90041-6

Lanir Y, Namani R (2015) Reliability of structure tensors in representing soft tissues structure. J Mech Behav Biomed Mater 46:222–228

Lebedev VI (1977) Spherical quadrature formulas exact to orders 25–29. Sib Math J 18(1):99–107. https://doi.org/10.1007/BF00966954

Lebedev VI (1975) Values of the nodes and weights of ninth to seventeenth order gauss-markov quadrature formulae invariant under the octahedron group with inversion. USSR Comput Math Math Phys 15(1):44–51. https://doi.org/10.1016/0041-5553(75)90133-0

Lebedev VI (1976) Quadratures on a sphere. USSR Comput Math Math Phys 16(2):10–24. https://doi.org/10.1016/0041-5553(76)90100-2

Li K, Ogden RW, Holzapfel GA (2018) Modeling fibrous biological tissues with a general invariant that excludes compressed fibers. J Mech Phys Solids 110:38–53

Li K, Holzapfel GA (2019) Multiscale modeling of fiber recruitment and damage with a discrete fiber dispersion method. J Mech Phys Solids 126:226–244

Lu J, Luo Y (2016) Solving membrane stress on deformed configuration using inverse elastostatic and forward penalty methods. Comput Methods Appl Mech Eng 308:134–150. https://doi.org/10.1016/j.cma.2016.05.017

Lu J, Zhou X, Raghavan M (2007) Inverse method of stress analysis for cerebral aneurysms. Biomech Model Mechanobiol 7:477–86. https://doi.org/10.1007/s10237-007-0110-1

Lu J, Hu S, Raghavan ML (2013) A shell-based inverse approach of stress analysis in intracranial aneurysms. Ann Biomed Eng 41(7):1505–1515. https://doi.org/10.1007/s10439-013-0751-4

Luo YM, Fan ZW, Baek S, Lu J (2018) Machine learning-aided exploration of relationship between strength and elastic properties in ascending thoracic aneurysm. Int J Numer Methods Biomed Eng. https://doi.org/10.1002/cnm.2977

Luo Y, Duprey A, Avril S, Lu J (2016) Characteristics of thoracic aortic aneurysm rupture in vitro. Acta Biomater 42:286–295. https://doi.org/10.1016/j.actbio.2016.06.036

Martufi G, Christian GT (2011) A constitutive model for vascular tissue that integrates fibril, fiber and continuum levels with application to the isotropic and passive properties of the infrarenal aorta. J Biomech 44(14):2544–2550

Martyn CN, Greenwald SE (1997) Impaired synthesis of elastin in walls of aorta and large conduit arteries during early development as an initiating event in pathogenesis of systemic hypertension. Lancet 350(9082):953–955. https://doi.org/10.1016/S0140-6736(96)10508-0

Rachev A, Shazly T (2019) A structure-based constitutive model of arterial tissue considering individual natural configurations of elastin and collagen. J Mech Behav Biomed Mater 90:61–72. https://doi.org/10.1016/j.jmbbm.2018.09.047

Rezakhaniha R, Agianniotis A, Schrauwen JT, Griffa A, Sage D, Bouten CV, van de Vosse FN, Unser M, Stergiopulos N (2012) Experimental investigation of collagen waviness and orientation in the arterial adventitia using confocal laser scanning microscopy. Biomech Model Mechanobiol 11(3–4):461–73. https://doi.org/10.1007/s10237-011-0325-z

Romo A, Badel P, Duprey A, Favre J-P, Avril S (2014) In vitro analysis of localized aneurysm rupture. J Biomech 47(3):607–616. https://doi.org/10.1016/j.jbiomech.2013.12.012

Rodrguez JF, Cacho F, Bea JA, Doblare M (2006) A stochastic-structurally based three dimensional finite-strain damage model for fibrous soft tissue. J Mech Phys Solids 54(4):864–886

Rodriguez JF, Alastrue V, Doblare M (2008) Finite element implementation of a stochastic three dimensional finite-strain damage model for fibrous soft tissue. Comput Methods Appl Mech Eng 197(9–12):946–958

Roy S, Boss C, Rezakhaniha RS, Stergiopulos N (2010) Experimental characterization of the distribution of collagen fiber recruitment. J Biorheol 24:84–93. https://doi.org/10.1007/s12573-011-0027-2

Sacks MS (2003) Incorporation of experimentally-derived fiber orientation into a structural constitutive model for planar collagenous tissues. J Biomech Eng 125(2):280–7. https://doi.org/10.1115/1.1544508

Simo JC, Taylor RL, Pister KS (1985) Variational and projection methods for the volume constraint in finite deformation elasto-plasticity. Comput Methods Appl Mech Eng 51(1):177–208. https://doi.org/10.1016/0045-7825(85)90033-7

Sokolis DP, Kritharis EP, Giagini AT, Lampropoulos KM, Papadodima SA, Iliopoulos DC (2012) Biomechanical response of ascending thoracic aortic aneurysms: association with structural remodelling. Comput Methods Biomech Biomed Eng 15(3):231–248. https://doi.org/10.1080/10255842.2010.522186

Sugita S, Matsumoto T (2013) Yielding phenomena of aortic wall and intramural collagen fiber alignment: Possible link to rupture mechanism of aortic aneurysms. J Biomech Sci Eng 8(2):104–113. https://doi.org/10.1299/jbse.8.104

Sugita S, Matsumoto T, Ohashi T, Kumagai K, Akimoto H, Tabayashi K, Sato M (2011) Evaluation of rupture properties of thoracic aortic aneurysms in a pressure-imposed test for rupture risk estimation. Cardiovasc Eng Technol. https://doi.org/10.1007/s13239-011-0067-1

Weisbecker H, Unterberger MJ, Holzapfel GA (2015) Constitutive modelling of arteries considering fibre recruitment and three-dimensional fibre distribution. J R Soc Interface 12(105):20150111. https://doi.org/10.1098/rsif.2015.0111

Wulandana R, Robertson AM (2005) An inelastic multi-mechanism constitutive equation for cerebral arterial tissue. Biomech Model Mechanobiol 4(4):235–248. https://doi.org/10.1007/s10237-005-0004-z

Wuyts FL, Vanhuyse VJ, Langewouters GJ, Decraemer WF, Raman ER, Buyle S (1995) Elastic properties of human aortas in relation to age and atherosclerosis: a structural model. Phys Med Biol 40(10):1577–1597. https://doi.org/10.1088/0031-9155/40/10/002

Zeinali-Davarani S, Wang Y, Chow MJ, Turcotte R, Zhang Y (2015) Contribution of collagen fiber undulation to regional biomechanical properties along porcine thoracic aorta. J Biomech Eng 137(5):051001. https://doi.org/10.1115/1.4029637

Zhou X, Raghavan ML, Harbaugh RE, Lu J (2010) Patient-specific wall stress analysis in cerebral aneurysms using inverse shell model. Ann Biomed Eng 38(2):478–489. https://doi.org/10.1007/s10439-009-9839-2

Zulliger MA, Fridez P, Hayashi K, Stergiopulos N (2004) A strain energy function for arteries accounting for wall composition and structure. J Biomech 37(7):989–1000. https://doi.org/10.1016/j.jbiomech.2003.11.026

Zulliger MA, Stergiopulos N (2007) Structural strain energy function applied to the ageing of the human aorta. J Biomech 40(14):3061–3069